12 Surface Physics

T. Greber, M. Hengsberger, J. Wider, H. J. Neff, W. Auwärter, F. Baumberger,
M. Hoesch, M. Muntwiler, I. Matsuda, R. Karrer, M. Barry, W. Deichmann, J. Osterwalder

Artificial nanostructures, exemplified e.g. by ultrathin films, quantum wires or quantum dots, are of enormous scientific and technological interest. Their electronic and magnetic properties are dominated by size- and shape dependent quantum effects and can thus be tailored to fulfill any particular need. Their diameter in at least one dimension does not exceed a few atomic layers, and therefore they consist to a large extent of interfaces and surfaces. In the surface physics laboratory we prepare clean surfaces, ultrathin films and nanostructures under ultrahigh vacuum (UHV) conditions and characterize their surface and interface structures at atomic resolution. Their electronic and magnetic properties are studied in detail. In order to measure the geometric arrangement of the atoms within the first few monolayers of the surface we apply predominantly electron-based techniques such as x-ray photoelectron diffraction (XPD), medium-energy electron diffraction (MEED), low-energy electron diffraction (LEED), and more recently also scanning-tunneling and atomic force microscopy (STM/AFM). Angle-resolved UV photoelectron spectroscopy (ARUPS) gives us a detailed picture of the electronic band structure of such systems. Specifically, our experimental setup permits to directly map sections through the Fermi surface, which describes the electronic degrees of freedom relevant for transport properties, magnetic interactions and phase transitions. An important asset of such experiments is that the same probe (photoemission) gives us structural, electronic and magnetic information, and we can therefore study the interplay between these different degrees of freedom on the same sample.

Over the past year we have continued our work on the following systems:
Vicinal Cu(111) surfaces expose (111)-oriented terraces separated by a roughly regular array of monoatomic steps, therefore they represent lateral nanostructures that can be easily prepared. We have studied the behaviour of the two-dimensional electron gas formed by a surface state in this well-defined and tunable potential energy landscape. In particular, we observed that the repulsive energy barriers represented by the clean steps are replaced by attractive potential wells when the steps are decorated with adsorbed carbon monoxide molecules (see Section 12.1). Moreover, in a collaboration with groups from the Technical University of Berlin and from Kansas State University, a solely optical technique was found to be sensitive to the detailed geometry of the steps (Section 12.2). As a photon-in photon-out technique, reflection anisotropy spectroscopy (RAS) is very attractive because it allows one to characterize microscopic surface properties under much less stringent conditions than the usual electron-based techniques that require UHV.

The quality and the electronic character of the interfaces are very important in metal-insulator heterojunctions, especially for magnetic devices based on junctions in which the tunneling barrier depends on the electron spin. A system which we continued to study thoroughly is the Ni(111) surface covered with one monolayer of hexagonal boron nitride (h-BN). In a collaboration with the Technical University of Vienna, it could be established by density functional theory that the magnetic moment per nickel atom is reduced at the interface, and based on the photoemission data a new reduction mechanism could be proposed (Section 12.3). An attempt to grow a regular array of linear metal-insulator-metal nanostructures based on a vicinal Ni(111) surface failed (Section 12.4). This study illustrates important pitfalls in materials science on the nanoscale.

In this last year we have also begun to investigate metal-semiconductor systems that form self-organizing nanostructures. When annealed at high temperature, the deposition of monolayer quantities of Cu on Si(111) leads to a discommensurate structure where a

two-dimensional metallic copper-silicide layer is organized in more or less regular 20 Å-size domains. In Section 12.5 it is described how the conduction electrons respond to this nanostructuring. On the same Si(111) surface, gold atoms can form linear chains. Our investigation of the electronic states near the Fermi energy reveals that these chains produce a one-dimensional surface state, but that this state does not cross the Fermi energy, i.e. these chains are not metallic wires (Section 12.6). A third metal-semiconductor interface, namely lead on Ge(111), has caught our attention because it exhibits a surface phase transition. In a collaboration with Tohoku University we have applied a promising new technique for measuring surface bond geometries inside this interface (Section 12.7).

Concurrent with these ongoing system-oriented studies, significant progress has been made in two projects related to the development of new experimental techniques:

The construction of our new spectrometer for spin-polarized Fermi surface mapping, which is designed to go eventually to the Surface and Interface Spectroscopy beamline of the Swiss Light Source (SLS), has been completed. First test experiments on a magnetized Ni(111) sample were highly successful (see Section 12.8). This experiment will permit the spin-resolved measurement of Fermi surfaces in magnetic nanostructures.

Our picosecond time-resolved electron diffraction experiment is now close to completion, with the ongoing implementation of the laser pulse amplifier that will deliver enough energy per pulse to produce significant transient temperature rises for each individual pulse (Section 12.9). The pulsed low-energy electron gun that has been designed and tested last year will be used for the first picosecond time-resolved LEED experiments revealing ultrafast structural changes at surfaces.

The near-node photoelectron holography spectrometer has been moved to the Surface and Interface Microscopy (SIM) beamline of the SLS where it will be used for studying adsorption geometries of biomolecules by direct holographic reconstruction. The group's activities at the Advanced Photoemission (APE) beamline at the ELETTRA synchrotron in Trieste, Italy, have been very limited during this past year due to continuing delays in the commissioning of the beam optics.

We have continued our collaboration with the surface chemistry group of Prof. J. R. Huber of the Physical Chemistry Department (P. Willmott, H. Spillmann) who have developed unique thin film preparation capabilities using pulsed reactive crossed-beam laser ablation. They have grown single crystalline films of zirconium carbonitrides (ZrC_xN_{1-x}) with the aim of correlating the hardness of these materials with their electronic structure as a function of the composition parameter x.

12.1   Tailoring confining barriers for surface states: CO/vicinal Cu(111)

in collaboration with B. Delley, Solid State Theory Group, Paul–Scherrer–Institut, Villigen, Switzerland

The clean Cu(111) surface supports a free electron like Shockley–type surface state, with a maximum binding energy of ~ 0.4eV at $\bar{\Gamma}$. This state arises as a consequence of the broken translational symmetry in the normal direction at the crystal surface. Its wave functions propagate parallel to the surface with a Fermi wave length of $\lambda_F \sim 3$nm. They fall off exponentially both towards the vacuum and towards the bulk and are thus quasi two-dimensional (2D). Monoatomic steps on an otherwise flat surface are known to act as repulsive potential barriers for surface state electrons [1]. Hörmandinger *et al.* showed that periodic arrays of steps, as present on a vicinal surface, are well described by a 1D model with rectangular potential barriers [2]. The superlattice leads to an enhanced effective mass perpendicular to

the steps, causing the elliptic Fermi surface contour observed on Cu(332) [3].
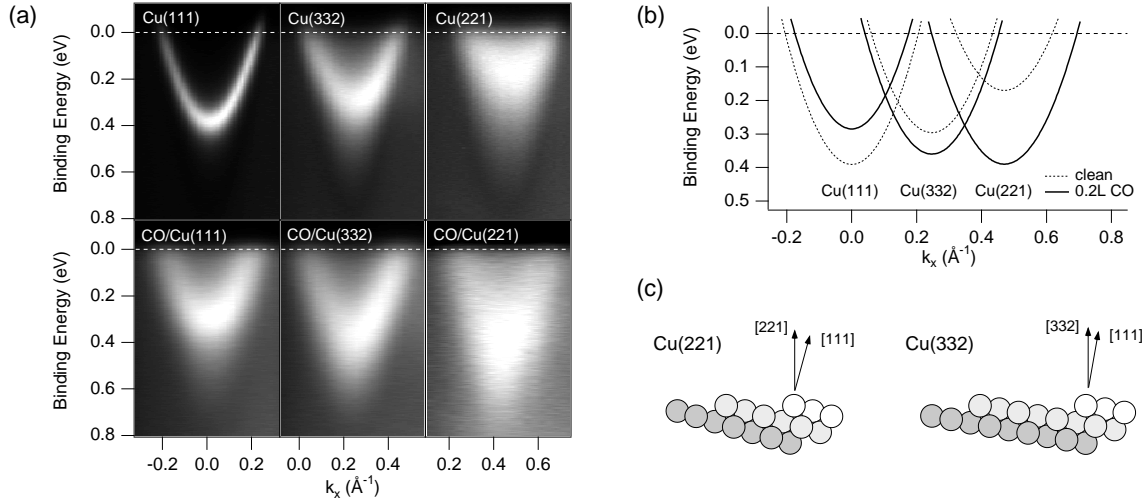

Figure 12.1: *(a) Measured photoemission dispersion plots (He Iα excitation), showing parabolic dispersion of the Shockley surface state on Cu(111) and two vicinal surfaces with and without CO adsorption (0.2L). (b) Compilation of the dispersion relations found on the clean (dotted lines) and CO-adsorbed (solid lines) surfaces, obtained from fitting the data shown in (a). (c) Hard sphere models of the two vicinal surfaces.*

We have investigated the change of the step potential after decoration with carbon monoxide. The CO molecules preferentially adsorb on top of the step atoms, and different ordered structures where steps sites are consecutively filled up to 0.75ML were observed by STM [4]. Photoemission dispersion plots for the clean and step decorated surfaces are shown in Fig. 12.1.

The energy shift ΔE of the band bottom in going from the flat (111) surface to the vicinal surfaces changes the sign with the adsorption of CO. In a 1D model, ΔE is given to first order by $\Delta E = U_0 a/\ell$, where $U_0 a$ is the integrated step potential and ℓ the terrace length. We thus conclude that the step potentials change the sign from being repulsive on the bare surfaces to attractive on the step decorated surfaces. Density functional calculations reveal that this effect is due to the very local change of the electrostatic potential at the adsorption site.

12.2   Reflection anisotropy spectroscopy (RAS) on vicinal Cu(111) surfaces

in collaboration with Th. Herrmann, N. Esser, W. Richter, Institut für Festkörperphysik, TU Berlin, Germany, and A. Kara, T. Rahman, Physics Department, Kansas State University, Manhattan U.S.A.

It is a main perspective of condensed matter research to link the microscopic electronic structure of surfaces with their macroscopic properties such as e.g. electrical resistance or hardness. Optical phenomena are governed by microscopic as well as macroscopic properties and are therefore a useful pilar for this bridge. In this context we performed reflection anisotropy spectroscopy (RAS) measurements on vicinal Cu(111) surfaces. The bulk contribution to the normal incidence reflectivity of a cubic crystal does not depend on the azimuthal orientation of the polarization vector. Therefore any anisotropy in reflection must stem from

an anisotropy in the surface. This makes RAS an optical method that is sensitive to the topmost atomic layers [5].

In Fig. 12.2b) the RA spectra for two vicinal surfaces with the two different step geometries (A and B type) are shown. The two types of steps can clearly be distinguished by RAS. The maximum difference between the two surfaces occurs at a photon energy of 4.2 eV. The reflection anisotropy is defined as $A = 2(R_\parallel - R_\perp)/(R_\parallel + R_\perp)$ where $R_\parallel$ and $R_\perp$
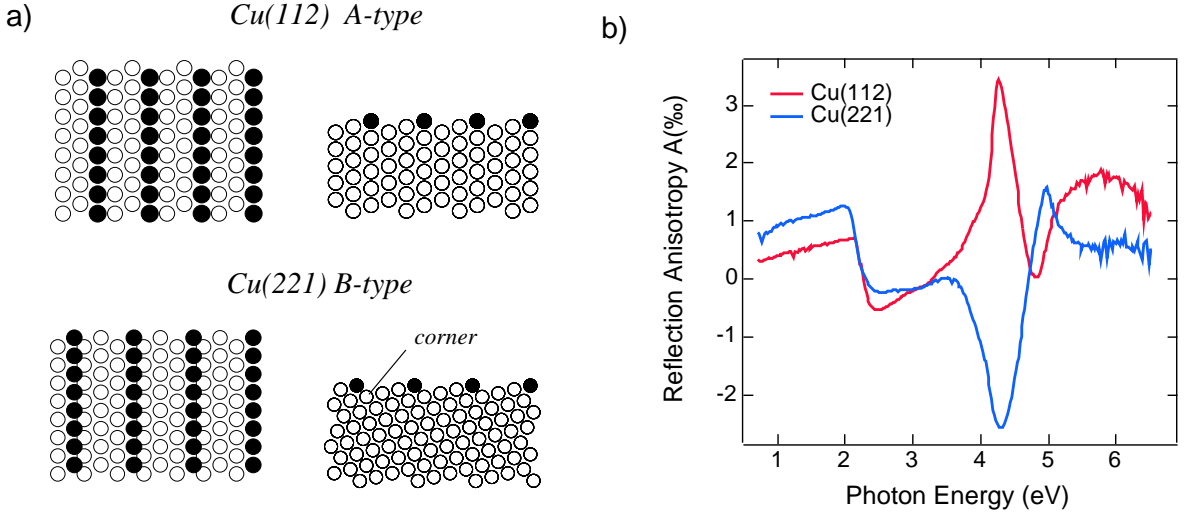

Figure 12.2: *Reflection anisotropy from Cu(112) and Cu (221). In a) the two vicinal surfaces are shown in a top and in a side view, where it becomes clear that the A type steps of Cu(112) consist of (001) facets, while the B type steps of Cu(221) are (111) facets. b) RA spectra in the photon energy range between 0.8 and 6.5 eV. The anisotropy A is largest at 4.2 eV and changes its sign in going from A to B type steps.*

are the amplitudes of the reflected light with polarization parallel or perpendicular to the steps. The maximum anisotropy is in the order of 3000 ppm. The penetration length of 4 eV (310 nm) light in copper is 18 nm or 86 layers. At a reflectivity of 33 % a single atom in the Cu(221) unit cell can therefore, in a simple atomic picture, contribute a maximum anisotropy of 0.8 %. There is one particular site in these vicinal surfaces that has a significantly different local environment: the corner atoms (see Fig. 12.2a)) have coordination numbers 10 or 11 in A and B type vicinals, respectively. Density functional calculations show that the corner atoms of A and B type steps have ellipsoidal charge density distributions with their long axis parallel or perpendicular to the steps. Within the model of Tarriba and Mochán [6] this may explain the dependence of the reflection anisotropy on the step geometry.

12.3   Reduction of the magnetic moment at the h-BN/Ni(111) interface

in collaboration with G. Grad and P. Blaha, Institut für Physikalische und Theoretische Chemie, TU Wien

Atomically sharp interfaces are a prerequisite for the realization of electronic and spintronic devices with ultimate performance. The single-layer system of hexagonal boron-nitride on nickel(111) is an ideal case for testing the concepts of spin-dependent electron scattering at interfaces. h-BN/Ni(111) is a perfect (1x1) commensurate interface, where the small lattice mismatch of 0.4% is compensated by a slight corrugation (0.1Å) of the h-BN layer [7]. The

influence of h-BN on the Ni magnetic moments is investigated by means of photoemission and density functional theory (DFT) [8].

Figure 12.3a) shows He Iα excited photoemission spectra for Ni(111) and h-BN/Ni(111) in normal emission. The most prominent features upon formation of the h-BN layer are the BN related σ and π bands at 5.3 and 10.0 eV binding energy. The work function shifts by 1.8 eV from 5.3 eV to 3.5 eV. This signals that the h-BN layer acts as an electron donor to the nickel substrate. The DFT calculations for a single (free-standing) layer of h-BN indicate a charge transfer of 0.56 electrons from boron to nitrogen. In the case of h-BN on Ni(111) a
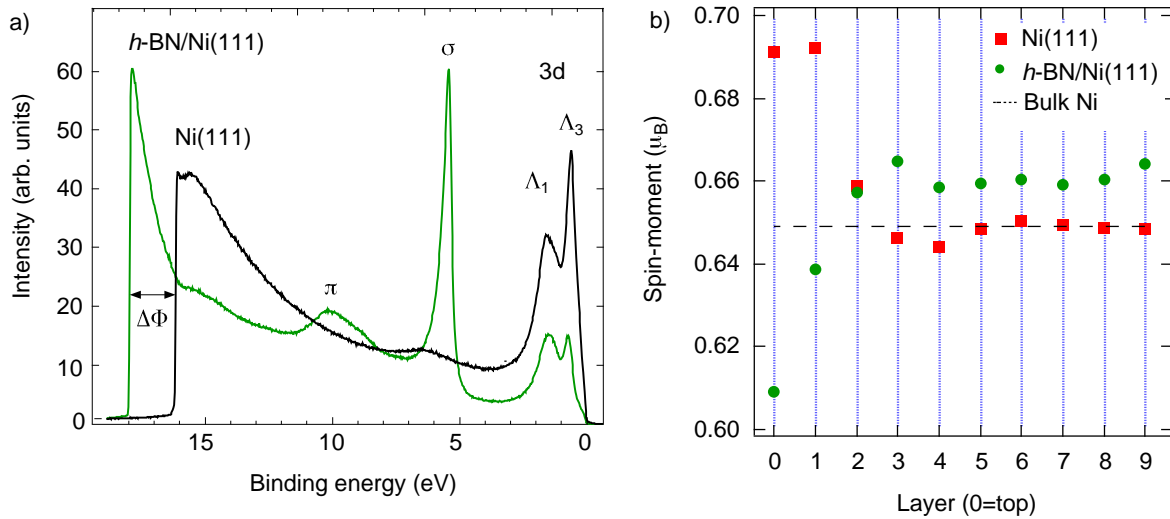

Figure 12.3: *a) Normal emission UP-spectra from Ni(111) and h-BN/Ni(111). b) Layer-resolved magnetic moment of Ni(111) and h-BN/Ni(111) as determined from DFT slab calculations.*

charge of 0.59 electrons on nitrogen and -0.65 e^- on boron is found. Therefore the net charge transfer to the substrate is 0.06 electrons per unit cell. Within an electrostatic picture where a charge separation length of 1Å is assumed this yields a work function shift of 2 eV which has the same sign and order of magnitude as the observation. The charge transfer is reflected as well in the energy down-shift of the Λ_3 d-band by 0.1 eV to 0.65 eV. In a rigid-band picture this shift is explained by charge transfer into empty bands of the substrate. This charge is mainly transferred into the minority Ni d-band since its density of states is much larger than that of the sp-bands. A decrease of the magnetic moment per Ni atom in the h-BN/Ni(111) interface is the consequence. Slab calculations support this picture and give a more precise, layer-dependent view of the magnetic moment near the interface. In Figure 12.3b) the layer-resolved spin moment, i.e. the difference of spin-up and spin-down charges inside atomic spheres of $R_{MT} = 2.3a_o$ are shown. For Ni(111) we find a bulk magnetic moment of $0.65\mu_B$ and the surface enhancement of the magnetic moment is 6%. The large 19 layer calculations do furthermore indicate Friedel type oscillations in the magnetic moment with an amplitude of less than 0.5% and a wavelength in the order of 3 to 4 layer spacings. For the case of h-BN/Ni(111) the magnetic moment in the top layer is reduced by $0.08\mu_B$ with respect to the Ni(111) top layer. The reduction of the magnetic moment induced by a charge transfer into unoccupied minority d-band states describes a mechanism that is qualitatively different from the hybridisation mechanism of Tersoff and Falicov [9].

12.4 Self-Organized 1D Nanostructures on Stepped Boron Nitride Films

On a flat Ni(111) surface h-BN can be grown as a compact commensurate monoatomic layer [10, 11]. With a second metallic phase grown on top of the h-BN, a well-defined model system for the study of metal-insulator-metal interfaces was prepared and investigated experimentally [12]. While it is known that on stepped metal surfaces one-dimensional atomic
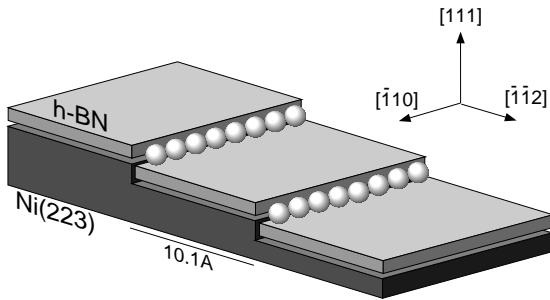
Figure 12.4: *Idealized model of a one-dimensional quantum wire on a stepped h-BN/Ni substrate.*

structures ("quantum wires") can be grown with elementary molecular beam epitaxy [13], this "step-decoration" growth mode has not yet been reported for a three-phase system like metal/h-BN/Ni. Our intention was to produce a sample close to the idealized model illustrated in Fig. 12.4 with the same methods and to examine its electronic structure. As substrate a nickel single-crystal cut along a (223) face is chosen. This surface ideally consists of 10.1 Å (4 2/3 atomic rows) wide (111) terraces separated by monoatomic steps. On this substrate a h-BN layer was expected to follow the steps of the substrate and allow step-decoration with a metal, e.g. copper or cobalt. Established preparation techniques (Ar ion sputtering, annealing of the substrate, catalytic growth of h-BN under borazine exposure, and molecular beam epitaxy with Cu) were applied until either a partial stage or completion of the Cu/h-BN/Ni(223) layered structure was reached. The prepared structures were characterized with regard to long-range step order (LEED) and h-BN film quality (XPS, UPS). As it was reported by Rokuta *et al.* for h-BN/Ni(755) [14], the surface strongly facets. The most
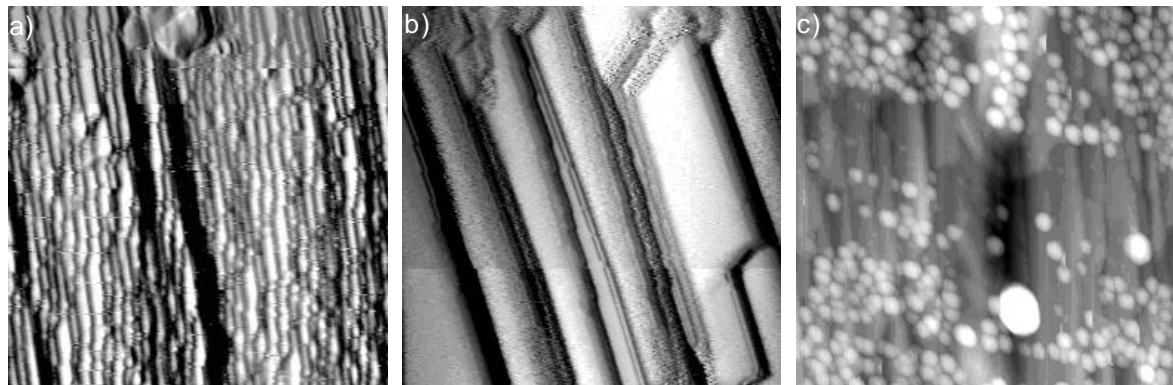
| 400 Å × 400 Å | 400 Å × 400 Å | 1000 Å × 1000 Å |

Figure 12.5: *STM measurements of different samples: (a) The vicinal Ni(223) surface shows narrow terraces with an average width of 10.7 Å. (b) After h-BN film growth terraces are up to 70 Å wide and separated in height by several atomic layers. (c) In the Cu/h-BN/Ni(223) image the wide BN/Ni terraces are visible in the background. The bright disks represent Cu islands, their apparent shape (height ≈ 8 Å (4 layers), width ≈ 35 Å) is a convolution with the STM tip.*

striking results were obtained with STM: Although a fairly good Ni(223) vicinal substrate
with narrow terraces could be prepared (Fig.12.5a), the terraces become much larger and
the steps significantly higher during h-BN film growth (Fig.12.5b). Furthermore, the terrace
width distribution gets much broader, and non-(111) facets show up.

The real situation with Cu evaporated onto h-BN/Ni(223) is shown in Fig.12.5c: The Cu
atoms aggregate to islands which are located in the terrace centers rather than close to step
edges. Their coordinates are correlated with the steps but they do not connect, and thus
do not form the desired one-dimensional nanostructures. The tendency of the h-BN/Ni(223)
system to step bunching, and the preferred growth of Cu islands on the terraces rather than
at the steps, are currently not understood.

12.5   The Fermi surface of a discommensurate surface layer

The growth of copper on Si(111) has attracted a lot of academic and technological attention
as a highly relevant metal-on-semiconductor interface. Maybe the most intriguing issue is
the well-defined and stable interface layer formed during elevated-temperature growth. This
layer exhibits a (5.55×5.55) periodicity that is not commensurate with the Si(111) substrate.
A recent structure model was brought forward by Zegenhagen *et al.* [15] and is depicted
in Fig. 12.6a). The main elements of this model are (i) an in-plane lattice constant of the
Cu_2Si layer that is expanded by 10 % relative to the underlying substrate, (ii) a rotation of
$\pm3°$ of the silicide lattice relative to the Si(111) lattice, and (iii) the formation of a more or
less regular pattern of silicide domains with about 20 Å diameter bounded by a dislocation
network. The local geometry within this two-dimensional silicide layer has recently been
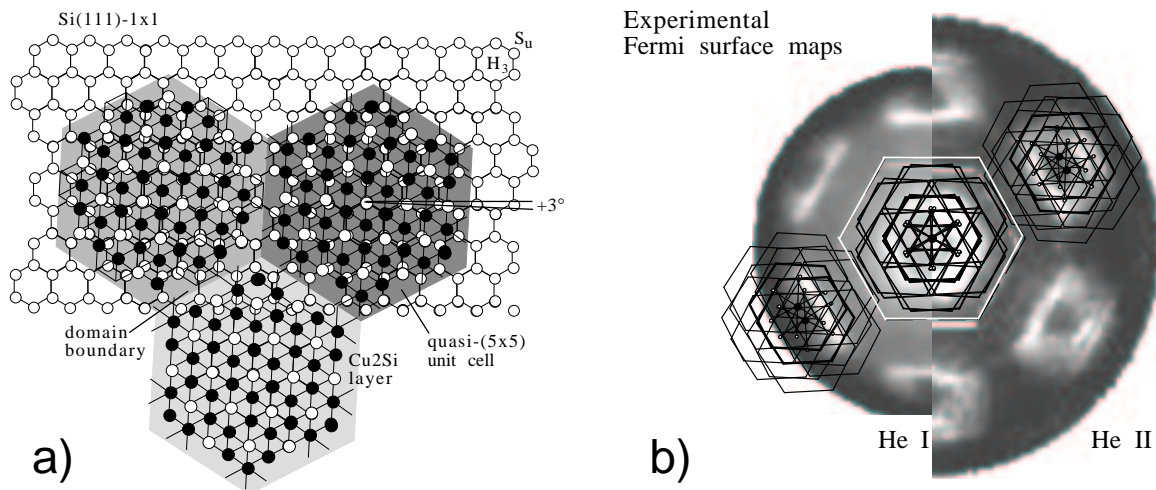confirmed by photoelectron diffraction experiments of our group [16].

Figure 12.6: *a) Schematic representation of the structural model for the discommensurate
quasi-5x5 Cu/Si(111) layer. b) Overlay of the schematic Fermi surface pattern, containing
all the structural elements of the model depicted in a), on the measured Fermi surface data
measured by He I and He II excitation. The two experimental intensity maps have been
brought to matching k-vector scales.*

In early photoemission experiments [17] we realized that this silicide layer is metallic, so
we engaged in a detailed study of how this unusual discommensurate structure is reflected
in the electronic structure and specifically in the Fermi surface. Fig. 12.6b) shows photo-
emission Fermi surface maps taken with He I and with He II radiation at photon energies

of 21.2 eV and 40.8 eV, respectively. The data show sharp contours that suggest a hexagonal Fermi surface spanning half the linear dimensions of the Si(111) (1×1) surface Brillouin zone. In addition, umklapp Fermi surface contours are seen, originating from electrons that have scattered off the regular network of discommensuration lines. The positions of these umklapp contours are consistent with all aspects of the Zegenhagen model described above, as is demonstrated by the overlay of the schematic Fermi surface contours that have been symmetry-expanded according to the structure model. This study thus gives a further confirmation of its correctness, and it demonstrates that the electrons in this metallic silicide layer have a coherence length - at room temperature - long enough to sample the full complexity of the discommensurate structure.

12.6   Fermi-surface and band mapping study of the Si(111)5x2-Au surface

Low-dimensional, especially one-dimensional (1D), structures induced by metal adsorption on semiconductor surfaces have attracted a considerable interest. They exhibit very in-
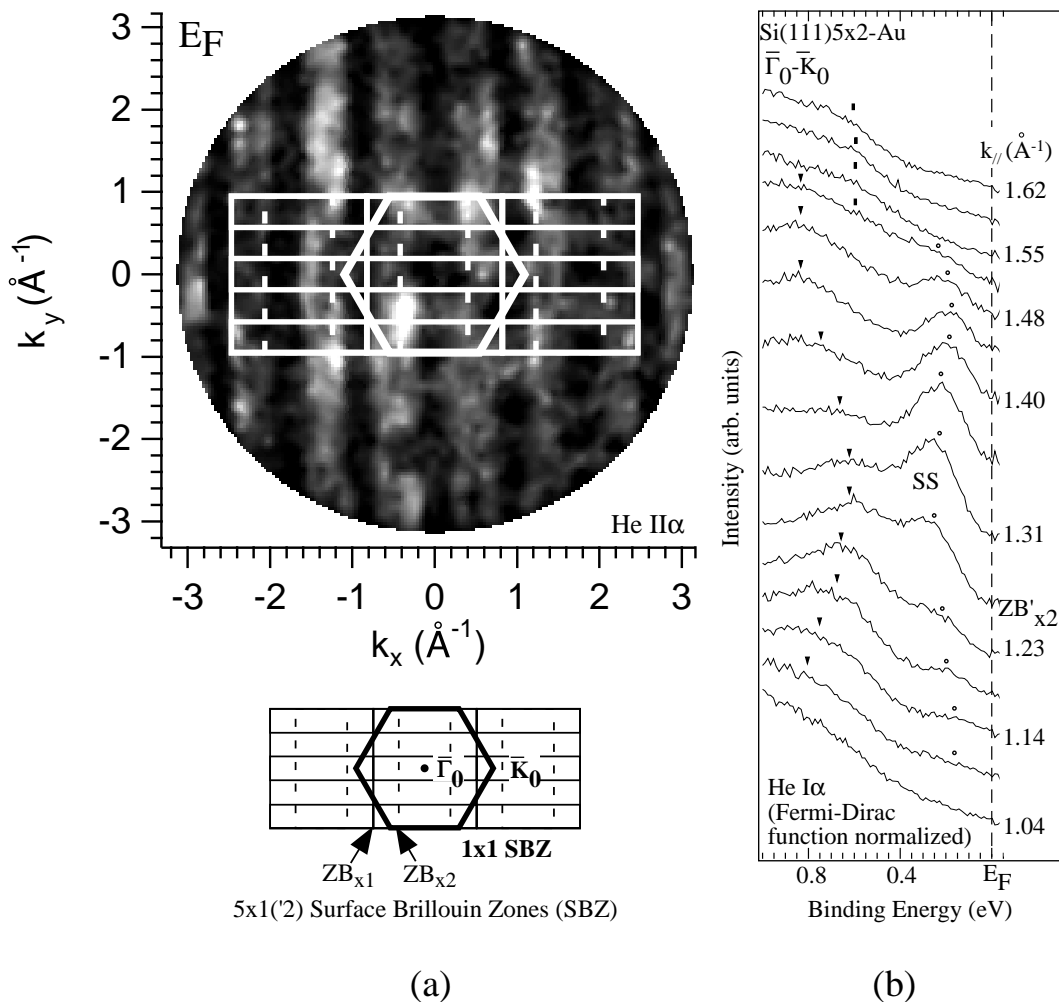

Figure 12.7: *(a) He IIα excited photoemission Fermi surface map and (b) He Iα excited ARPE spectra (normalized by the Fermi-Dirac distribution) from a single-domain Si(111)5x2-Au surface. The surface Brillouin zones and high symmetry points are indicated. The Au chains run along the horizontal (x) direction.*

triguing electronic properties due to increased interactions and subsequent correlations as a result of the electron confinement. Even though 1D *metallic* systems represent maybe the most interesting case, only few among the numerous varieties of the low-dimensional metal/semiconductor structures studied so far were reported to exhibit metallicity [19, 20]. The Si(111)5x2-Au surface is one such example according to a recent angle-resolved photo-emission spectroscopy (ARPES) study [21]. However, the ARPES data were taken with low energy resolution and the electronic structure near the Fermi level is still not well established [21]. More recently, a "pseudo-gap" of 300 meV at the Fermi level has been reported [22], raising again the question of the metallic character of the observed Au chains.

We have carried out detailed Fermi surface and band mapping measurements with high-resolution ARPES. The goal of this project was to study the electronic structure of the (single-domain) Si(111)5x2-Au surface near the Fermi level, which governs the thermodynamical properties, and to map directly the Fermi surface, which has not been investigated so far. Fig. 12.7(a) shows the resulting Fermi surface contours obtained with He IIα excitation with the 5x1(2) surface Brillouin zones (SBZ) superimposed. One can observe perfectly straight 1D features along the zone boundaries of SBZ$_{5\times2}$. At first glance, the result seems to confirm the previous proposal of a quasi-1D metal. However, through a detailed analysis of the spectra, we find that the apparent Fermi surface can be attributed to a broadening of ARPES signals from a 1D surface state just below the Fermi level. Figure 12.7(b) shows the Fermi-Dirac normalized ARPE spectra taken with He Iα photons. These data reveal that the 1D surface state (SS) that is responsible for the observed Fermi surface contours in Fig. 12.7(a) is *not* crossing the Fermi level. Thus, contrary to the previous understanding, the Si(111)5x2-Au surface is found to be non-metallic but semiconducting with 1D surface states just below the Fermi level, maybe due to a periodic lattice distortion within the Au chains. The present results are expected to contribute to our understanding of instabilities in low-dimensional systems.

12.7   Correlated Thermal Diffuse Scattering (CTDS) from Pb/Ge(111)

in collaboration with T. Abukawa and S. Kono, Research Institute for Scientific Measurements, Tohoku University, Sendai, Japan

Correlated Thermal Diffuse Scattering (CTDS) is a new structural tool for the detection of surface bonds, recently introduced and developed by a group at Tohoku University [23]. The Fourier transform of oscillations in the three dimensional (multiple-energy) diffraction pattern of medium-energy electrons reveals the surface Patterson function, i.e. bond lengths and bond angles within the surface layers. The Patterson function is derived directly from the experimental data, i.e. without assuming a model structure. Although the experimental setup is very similar for CTDS and low-energy electron diffraction (LEED), the two methods are complementary. LEED probes the *surface periodicities* whereas CTDS reveals information on the *local geometries* within the unit cell. The loss of surface sensitivity due to higher electron energies used for CTDS can partly be regained by chosing grazing incidence and/or excidence of the electrons. By chosing the appropriate scattering geometry, a specific bond direction can be emphasized in the Patterson function. We want to use this method for studying structural changes within the surface when a temperature dependent phase transition is crossed.

An example of CTDS measurements from the Pb/Ge(111) surface is shown in Fig. 12.8. At a coverage of 1/3 monolayer, this system exhibits an interesting phase transition around 250 K that has been associated with the formation of a surface charge density wave [24]. Interesting surface bonds are the tetrahedral Ge-Ge bond (yellow in Fig. 12.8a)) and the Ge-
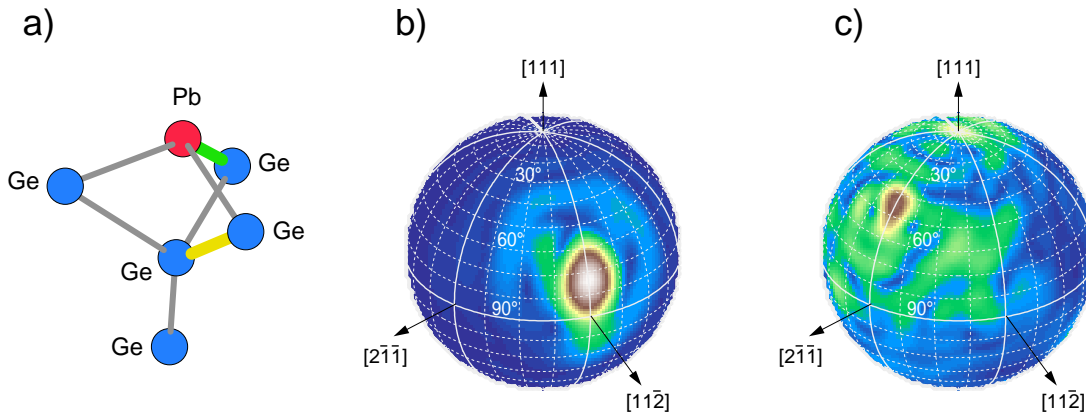
Figure 12.8: *CTDS measurements of the Pb/Ge(111)-$\sqrt{3}\alpha$-surface. a) Bonding geometry of the Pb/Ge surface. Pb atoms occupy T_4 sites above the truncated Ge lattice. The Ge-Ge tetrahedral bond and the Ge-Pb adatom bond are highlighted in yellow and green, respectively. b) Shell with radius 2.45 Å through the Patterson function displaying the Ge-Ge tetrahedral bond. c) Shell with radius 3.05 Å displaying the Ge-Pb adatom bond.*

Pb adatom bond determined by the adsorption geometry of the Pb adatom on the Ge surface (green in Fig. 12.8a)). Cuts through the experimental Patterson function (Figs. 12.8b) and c)) demonstrate that both surface bonds are clearly resolved. The elongation of the peaks along [111] can be explained by the relaxation of the surface which leads to a "distortion" of the surface bonds. The experimental Patterson function displays the superposition of the variety of these distorted bonds. The accuracy of the CTDS method is 0.1 Å and 1° in bond length and bond angle, respectively.

12.8 First experiments with COPHEE

in collaboration with V.N. Petrov, St. Petersburg Technical University, Russia

First experiments have been performed with COPHEE, the COmplete PHotoEmission Experiment on the Ni(111) surface. The COPHEE instrument is a high resolution photoelectron spectrometer with spin resolution, which has been taken into operation in 2001. The principle of operation is shown in Fig. 12.9. Photoelectrons emitted by VUV radiation from a sample are angle and energy selected by an electron lens and a hemispherical energy analyzer. The beam is then transported into one of two Mott detectors, which analyze the spin polarization [25]. A symmetric two-way deflector switches the beam periodically ($\approx$ 1 Hz) between the two Mott detectors to allow quasi simultaneous data collection. Each of the Mott polarimeters has two pairs of energy-selective detectors which count the electrons that are elastically backscattered at 50 keV from a gold foil, and therefore analyses two components of the polarization vector transverse to the incoming beam axis. In an electrostatic beam transport system the spin remains fixed in space and the two orthogonally arranged polarimeters cover all three axes and thus allow the complete measurement of the spin polarization vector. In a Fermi-surface mapping experiment using photoemission with a fixed light source and detector, the angular distribution of photoelectrons above the sample surface is measured by rotating the sample about two axes to cover all emission angles. In a magnetized sample, also the magnetization axis sweeps the whole hemisphere and therefore a three-dimensional
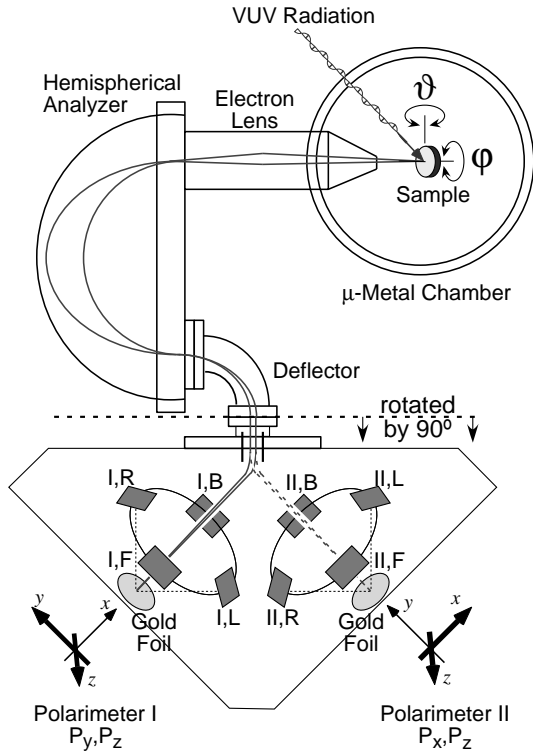
Figure 12.9: *Schematic view of COPHEE. Electrons photoemitted from a sample by UV radiation are energy- and angle-selected by an electrostatic analyzer and detected in two orthogonal Mott polarimeters. In an electrostatic beam deflection system the spin direction is conserved and polarimeter I measures the polarization components P_y and P_z, while polarimeter II measures P_x and P_z. The beam is switched between the two to allow quasi-simultaneous data collection. The polarimeter system is shown rotated by $90°$ for graphical clarity.*

polarimeter is necessary. In this sense COPHEE merits its ambitious name, because it measures all degrees of freedom of the photoelectron in the sample coordinates, *i.e.* the energy, momentum and spin.

12.8.1   Spin-resolved Fermi-surface mapping on Ni(111)

For the first experiments a newly developed magnetizable Ni(111) sample in a picture frame geometry was used. Because the Ni sample forms a closed loop, a sizable remnant in-plane magnetization can be achieved and stray fields are reduced. First the magnetization direction was determined directly by measuring the spin polarization vector of secondary electrons in normal emission upon excitation with UV light from a helium lamp. These electrons are polarized ($P \simeq 8\%$ for a fully magnetized sample [26]) through spin dependent scattering processes in the sample with the direction of polarization along the magnetization axis. The degree of magnetization of our sample was estimated to be 15 to 25 %. For further information see [27].

The Fermi-surface of nickel features sheets due to minority *d*-bands and a large *sp*-band electron surface. On the Ni(111) surface, a pair of spin-split *sp*-bands is seen around the $[\bar{1}\bar{1}2]$ azimuth with a pair of *d*-bands near by. In this geometry the two Mott detectors measure the spin-polarisation almost equivalently and a direct cross checking is possible. Fig. 12.10 shows spin-resolved photoemission data. The spin-character of the band is clearly revealed through the sign of the Mott detector asymmetry. The two asymmetry curves were measured quasi-simultaneously by 2 Hz switching between the two detectors. They fall precisely on top of each other.

12.9   Time-resolved electron diffraction

This project aims at the study of atom dynamics on solid surfaces near phase transitions. In the vicinity of the critical temperature T_c fluctuations in the order parameter are expected
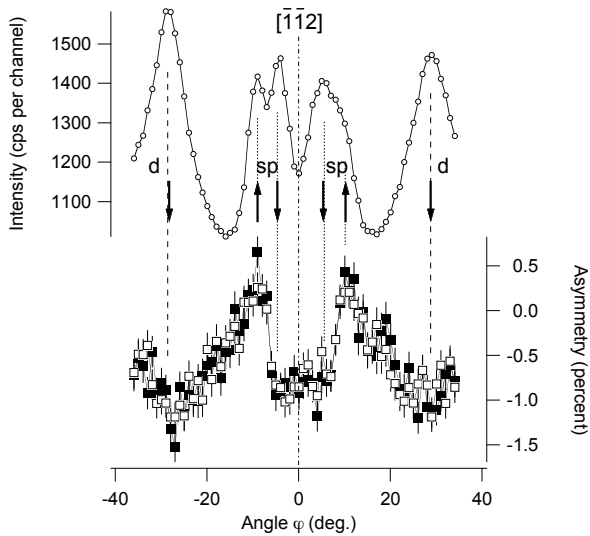
Figure 12.10: *Spin-resolved photoemission data from Ni(111) excited with HeIα radiation (hν = 21.2 eV). The upper part shows the photoelectron intensity and the lower part the measured asymmetry as a function of the azimuthal emission angle φ near grazing emission. Black arrows mark the known assignment of the peaks to (minority) d-bands and spin-split sp-bands. Scattering asymmetries from two Mott detectors (polarization component P_z) are shown by black and white squares.*

to occur, which should be reflected in the structural arrangement of the surface atoms. Two electron diffraction methods have been adopted allowing the appropriate parameter (local or long-range order) to be measured:

At medium kinetic energy (typ. 1 keV), broad oscillations appear in the diffuse background of the diffraction pattern, from which the local environment of the surface atoms can be extracted by numerial Fourier transform (Correlated Thermal Diffuse Scattering, CTDS, see section 12.7).

At low energy, (typ. 100 eV) the long-range periodicity of the surface is probed (Low-Energy-Electron Diffraction, LEED).

The necessary equipment has been developed and thoroughly tested in 2001. In particular, a 5 picosecond pulsed gun for low-energy electrons, which was built recently in our group [28] (see Annual Report 2000/2001), has been shown to provide bunches of electrons coherent enough for allowing diffraction patterns to be recorded [29].

Real-time measurements on a picosecond time scale will be effectuated in a pump-probe setup (see Fig 12.11): A train of 800 nm photon pulses from a laser oscillator is split into two, one of the branches being guided via a delay stage to the vacuum chamber and focused onto the sample (pump pulse). The sample, held below and close to T_c by use of a cryostat, is transiently heated above T_c by absorbing the light pulse and crosses again the phase transition during the subsequent cooldown. The photoelectron pulse, produced in the electron gun by frequency-doubled photons from the second branch, probes the surface structure at a certain time after the pump pulse. Using the delay stage this retardation can be varied, allowing the structural evolution after the pump pulse to be followed as a function of delay time.

The realization of this ambitious project, which has been in its final design stage in 2001, is in progress now and will be finished in spring 2002 : The laser system will be upgraded by a pulse amplifier, which will provide enough energy per pulse to obtain a significant temperature rise of a few tens of degree Kelvin in the sample surface area seen by the probing electrons. As a consequence a larger optical table top had to be ordered, and the new optical setup had to be planned. Moreover, since one single experiment will run over up to 30 hours, data acquisition and experiment control are automated. The hardware, necessary to pilot delay stage and CCD camera and to record all crucial experimental parameters like, e.g., sample temperature and laser power, was installed and tested. The software is currently being developed using Visual Basic language on a remote personal computer.
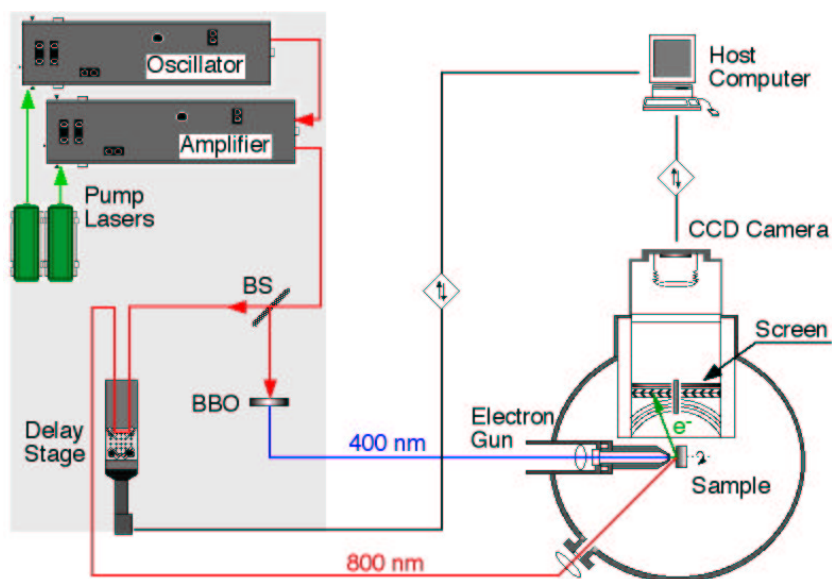
Figure 12.11: *Schematic view of the final experimental setup: Pulses from the laser oscillator are amplified and split (BS) into two branches; one branch (800 nm) leads via a delay stage to the vacuum chamber and is focused onto the sample; photons of the second branch are frequency doubled in a BBO crystal and used to produce photoelectrons in the electron gun. Electrons backreflected from the sample are amplified and detected on a fluorescent screen. The diffraction patterns are recorded by using a CCD camera coupled to a host computer.*

References

[1] M.F. Crommie, C.P. Lutz and D. M. Eigler, Science **262**, 218 (1993).

[2] G. Hörmandinger and J.B. Pendry, Phys. Rev. B **50**, 18607 (1994).

[3] F. Baumberger, T. Greber, and J. Osterwalder, Phys. Rev. B, **64**, 195411 (2001).

[4] G. Meyer, B. Neu, K.H. Rieder, Chem. Phys. Lett. **240**, 379 (1995).

[5] D.E. Aspnes, J.P. Harbison, A.A. Stunda and L.T. Florez, Phys. Rev. Lett. **59**, 1687 (1987).

[6] J. Tarriba and Luis Mochán, Phys. Rev. B **46**, 12902 (1992).

[7] W. Auwärter, T. J. Kreutz, T. Greber and J. Osterwalder, Surf. Sci. **429**, 229 (1999).

[8] P. Blaha, K. Schwarz and J. Luiz, WIEN 97, TU Vienna, 1997, Updated UNIX version of the Wien code as published by P. Blaha, K. Schwarz P. Sorantin, S. B. Tickey in Comput. Phys. Commun. **59**, 399 (1990).

[9] J. Tersoff and L.M. Falicov, Phys. Rev. B **26**,6186 (1982).

[10] Y. Gamou, M. Terai, A. Nagashima, and C. Oshima, Sci. Rep. RITU **A44**, 211 (1997).

[11] W. Auwärter, T. J. Kreutz, T. Greber, and J. Osterwalder, Surf. Sci. **429**, 229 (1999).

[12] W. Auwärter, M. Muntwiler, T. Greber, and J. Osterwalder, Surf. Sci., in press (2002).

[13] F. J. Himpsel, T. Jung, and J. E. Ortega, Surf. Rev. Lett. **4**, 371 (1997).

[14] E. Rokuta, Y. Hasegawa, A. Itoh, K. Yamashita, T. Tanaka, S. Otani, C. Oshima, Surf. Sci. **427-428**, 97 (1999).

[15] J. Zegenhagen, P. F. Lyman, M. Böhringer, M. J. Bedzyk, Phys. Status Solidi B **204**, 587 (1997).

[16] M. De Santis, M. Muntwiler, J. Osterwalder, G. Rossi, F. Sirotti, A. Stuck, L. Schlapbach, Surf. Sci. **477**, 179 (2001).

[17] M. De Santis, A. Stuck, J. Osterwalder, F. Sirotti, G. Rossi, Vuoto **21**, 200 (1991).

[18] H.-J. Neff, I. Matsuda, M. Hengsberger, F. Baumberger, T. Greber, J. Osterwalder, Phys. Rev. B **64**, 235415 (2001).

[19] P. Segovia, D. Purdie, M. Hengsberger, and Y. Baer, Nature (London) **402**, 504 (1999).

[20] H.W. Yeom, S. Takeda, E. Rotenberg, I. Matsuda, K. Horikoshi, J. Schaefer, C.M. Lee, S.D. Kevan, T. Ohta, T. Nagao, and S. Hasegawa, Phys. Rev. Lett. **82**, 4898 (1999).

[21] I.R. Collins, J.T. Moran, P.T. Andrews, R. Cosso, J.D. O'Mahony, J.F. McGilp, and G. Margaritondo, Surf. Sci. **325**, 45 (1995).

[22] K.N. Altmann, J.N. Crain, A. Kirakosian, J.-L. Lin, D.Y. Petrovykh, and F.J. Himpsel, Phys. Rev. B **64**, 035406 (2001).

[23] T. Abukawa, C.M. Wei, T. Hanano, and S. Kono, Phys. Rev. Lett. **86**, 335 (1999).

[24] J. M. Carpinelli, H. H. Weitering, E. W. Plummer, R. Stumpf, Nature (London) **381**, 398 (1996).

[25] V. N. Petrov, M. Landolt, M. S. Galaktionov, B. V. Yushenkov, Rev. Sci. Instrum. **68**, 4385 (1997).

[26] M. Landolt *Spin Polarized Secondary Electron Emission from Ferromagnets* in *Polarized Electrons in Surface Science*, ed. R. Feder, World Scientific, Singapore 1985.

[27] M. Hoesch, T. Greber, V. N. Petrov, M. Muntwiler, M. Hengsberger, W. Auwärter, J. Osterwalder, J. Electron Spectrosc. Relat. Phenom., in press (2002).

[28] R. Karrer, *Bau einer Elektronenkanone für zeitaufgelöste Beugung mit langsamen Elektronen*, Diplomarbeit, Universität Zürich, 2000.

[29] R. Karrer, H.J. Neff, M. Hengsberger, T. Greber, and J. Osterwalder, Rev. Sci. Instrum. **72**, 4404 (2001).